










# Magnetic refrigeration material operating at a full temperature range required for hydrogen liquefaction

Xin Tang<sup>1,2</sup>, H. Sepehri-Amin <sup>1,3✉</sup>, N. Terada <sup>1</sup>, A. Martin-Cid <sup>4</sup>, I. Kurniawan <sup>1,5</sup>, S. Kobayashi <sup>4</sup>, Y. Kotani <sup>4</sup>, H. Takeya<sup>1</sup>, J. Lai<sup>1</sup>, Y. Matsushita <sup>1</sup>, T. Ohkubo<sup>1</sup>, Y. Miura<sup>1</sup>, T. Nakamura <sup>1,3,4</sup> & K. Hono <sup>1,5</sup>

Magnetic refrigeration (MR) is a key technique for hydrogen liquefaction. Although the MR has ideally higher performance than the conventional gas compression technique around the hydrogen liquefaction temperature, the lack of MR materials with high magnetic entropy change in a wide temperature range required for the hydrogen liquefaction is a bottle-neck for practical applications of MR cooling systems. Here, we show a series of materials with a giant magnetocaloric effect (MCE) in magnetic entropy change ( $-\Delta S_m > 0.2 \text{ J cm}^{-3} \text{ K}^{-1}$ ) in the Er(Ho)Co<sub>2</sub>-based compounds, suitable for operation in the full temperature range required for hydrogen liquefaction (20–77 K). We also demonstrate that the giant MCE becomes reversible, enabling sustainable use of the MR materials, by eliminating the magneto-structural phase transition that leads to deterioration of the MCE. This discovery can lead to the application of Er(Ho)Co<sub>2</sub>-based alloys for the hydrogen liquefaction using MR cooling technology for the future green fuel society.

<sup>1</sup>National Institute for Materials Science, Tsukuba 305-0047, Japan. <sup>2</sup>International Center for Young Scientists, National Institute for Materials Science, Tsukuba 305-0047, Japan. <sup>3</sup>International Center for Synchrotron Radiation Innovation Smart (SRIS), Tohoku University, Sendai 980-8577, Japan. <sup>4</sup>Japan Synchrotron Radiation Research Institute, SPring-8, 1-1-1 Kouto, Sayo 679-5198, Japan. <sup>5</sup>Graduate School of Science and Technology, University of Tsukuba, Tsukuba 305-8577, Japan. ✉email: [h.sepehriamin@nims.go.jp](mailto:h.sepehriamin@nims.go.jp)

Magnetic materials undergo isothermal magnetic entropy changes ( $\Delta S_m$ ) or adiabatic temperature changes ( $\Delta T_{ad}$ ) upon the application or removal of an external magnetic field. This phenomenon is known as the magnetocaloric effect (MCE)<sup>1</sup>. Magnetic refrigeration (MR) based on the MCE is considered to be a promising energy-efficient and environmentally benign refrigeration technology<sup>2</sup>. The concept of cooling by adiabatic demagnetisation at the ultra-low temperatures was proposed independently by Debye<sup>3</sup> and Giauque<sup>4</sup> based on thermodynamic studies in the late 1920s. This concept was experimentally demonstrated in the early 1930s by Giauque and MacDougall on the adiabatic demagnetisation of  $Gd_2(SO_4)_3 \cdot 8H_2O$ , leading to attainment of temperatures below 1K<sup>5</sup>. The operation of MR can be also extended to room temperature application using magnetic refrigerants, such as  $Gd_5Si_2Ge_6$ <sup>6–8</sup>,  $(Mn,Fe)_2P_9$ ,  $MnAs$ <sup>10,11</sup>, Ni-Mn-based Heusler alloy<sup>12,13</sup> and  $La(Fe,Si)_{13}H$ <sup>14–16</sup>. Recently, the global demand for the reduction of CO<sub>2</sub> emission has increased the attention devoted to the use of renewable energy for which hydrogen plays an important role in the so-called decarbonised hydrogen society<sup>17</sup>. In this context, magnetic refrigeration has been demonstrated to be a potential candidate for hydrogen liquefaction and avoidance of hydrogen boil-off during storage<sup>18</sup>. In this approach, hydrogen gas is cooled to ~77 K (boiling temperature of liquid nitrogen) followed by a further decrease in temperature to its liquefaction temperature of 20 K. Because the existing magnetic refrigerant materials cannot maintain a large MCE over the wide temperature span of 77–20 K, a series of refrigerant materials are used in an active magnetic regenerator (AMR) system (Fig. 1a).

The isothermal magnetic entropy change ( $\Delta S_m$ ) is given by

$$\Delta S_m = \mu_0 \int_H^0 \left( \frac{\partial M}{\partial T} \right)_H dH \quad (1)$$

and is used to characterise the magnetocaloric response of a magnetic refrigerant, where  $\mu_0$  is the permeability of free space,  $M$  is the magnetisation,  $T$  is the temperature, and  $H$  is the external magnetic field. The maximum value of  $\Delta S_m$  is achieved near the magnetic transition temperature ( $T_{tr}$ ) owing to the large value of  $\frac{\partial M}{\partial T}$ .  $HoAl_2$  compound is one of the potential magnetic refrigerant materials for hydrogen liquefaction, which has  $-\Delta S_m = 0.16 \text{ J cm}^{-3} \text{ K}^{-1}$  at temperature of 32 K obtained from a single crystal and is called as a material with a giant MCE<sup>1,19</sup>. To realise an efficient AMR system for H<sub>2</sub> liquefaction applications, a larger magnetic entropy change of  $-\Delta S_m > 0.2 \text{ J cm}^{-3} \text{ K}^{-1}$  covering a broad temperature range of 20–77 K for magnetic refrigerants is needed. Giant MCEs ( $-\Delta S_m > 0.2 \text{ J cm}^{-3} \text{ K}^{-1}$ ) have been realised in Ho-based compounds (Fig. 1b), such as  $HoB_2$ <sup>20</sup>,  $HoNi_2$ <sup>21,22</sup>, and  $HoNi_2$ <sup>23,24</sup> at temperatures below 20 K. These ferro/paramagnetic phase transitions without thermal hysteresis have been classified as second-order magnetic phase transitions (SOPT). SOPT materials without thermal hysteresis intrinsically lead to reversible MCE and mechanical stability during cyclic performance<sup>25,26</sup>, and hence are desirable for practical application. To meet the requirements of AMR, giant MCE must be maintained at temperatures up to 77 K. However, the increase in  $T_{tr}$  of SOPT materials has been found to be achieved at the expense of  $|\Delta S_m|$ . For example,  $|\Delta S_m|$  values of  $0.17 \text{ J cm}^{-3} \text{ K}^{-1}$  and  $0.15 \text{ J cm}^{-3} \text{ K}^{-1}$  are obtained at 30 K for the  $(Gd_xHo_{1-x})B_2$  and  $HoAl_2$  compounds<sup>27,28</sup>, respectively, and  $|\Delta S_m|$  decreases to  $0.10 \text{ J cm}^{-3} \text{ K}^{-1}$  at 60 K for the  $DyAl_2$  compound<sup>28</sup>. Hence, there are very few refrigerant materials exhibiting a giant MCE of  $|\Delta S_m| > 0.2 \text{ J cm}^{-3} \text{ K}^{-1}$  that do not show thermal hysteresis at the temperatures of 30–77 K required for H<sub>2</sub> liquefaction in AMR systems. By contrast, magnetic

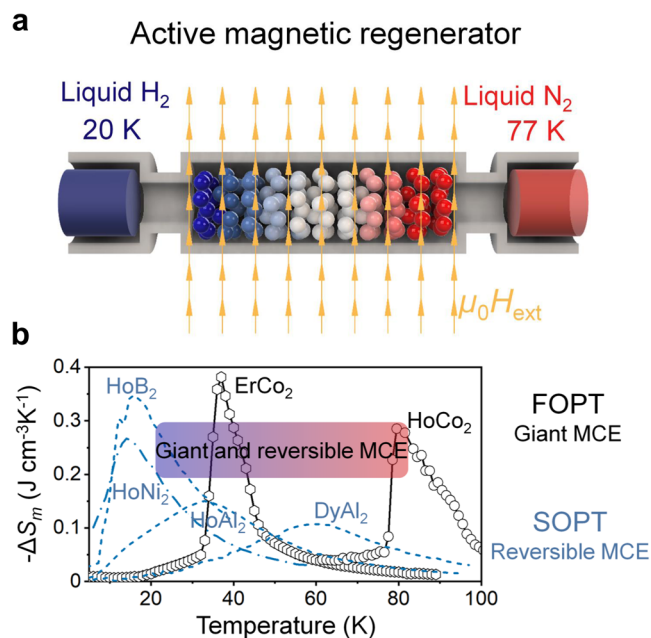


**Fig. 1** Magnetic refrigeration materials required for hydrogen liquefaction using magnetic refrigeration. **a** Schematic of the active magnetic regenerator for hydrogen liquefaction. A series of magnetic refrigerants with tailored transition temperatures at external field ( $\mu_0 H_{ext}$ ) are required to cover the large temperature range from the boiling temperature of nitrogen (77 K) to the boiling temperature of hydrogen (20 K). **b** Isothermal magnetic entropy change ( $-\Delta S_m$ ) as a function of temperature. Second-order magnetic phase transition materials illustrated by dashed blue curves, for example,  $HoB_2$ <sup>20</sup>,  $HoNi_2$ <sup>24</sup>,  $HoAl_2$ <sup>28</sup>, and  $DyAl_2$ <sup>28</sup> show no hysteresis, a giant MCE only at temperatures below 20 K and small MCE at temperatures above 30 K. First-order magnetic phase transition materials indicated by black curves with symbols exhibit giant magnetocaloric effects (MCEs) (large  $-\Delta S_m$ ) at a broad temperature range but with thermal hysteresis near the transition temperature, resulting in irreversible giant MCEs. Therefore, giant and reversible MCEs with broad operating temperature window illustrated by gradient colour from red to blue corresponding to the magnetic refrigerants with different transition in (a) from 77 K to 20 K are desirable for active magnetic regenerator.

refrigerant materials with first-order magnetic phase transition (FOPT) have giant MCEs induced by their magnetostructural phase transitions. For example, in  $ErCo_2$ , a transformation from the paramagnetic phase (cubic) to the ferrimagnetic phase (rhombohedral) results in  $-\Delta S_m = 0.37 \text{ J cm}^{-3} \text{ K}^{-1}$  at 37 K (Fig. 1b)<sup>29</sup>. With Ho substitution for Er,  $T_{tr}$  can be increased to 80 K while maintaining a giant MCE ( $-\Delta S_m > 0.2 \text{ J cm}^{-3} \text{ K}^{-1}$ ) in the  $(Ho_{1-x}Er_x)Co_2$  compounds<sup>30</sup>. However, the  $(Ho_{1-x}Er_x)Co_2$  compounds undergoing FOPT suffer from thermal hysteresis resulting in an irreversible MCE and mechanical instabilities<sup>25,26</sup>, hindering their application for AMR.

In this work, we demonstrate that for  $(Ho)ErCo_2$  compounds, the substitution of Co by particular 3d metal elements, such as Fe or Fe + Ni, can eliminate the hysteresis by avoiding the structural transformation, while maintaining a giant MCE at the transition temperature. Different from the conventional reports, the narrow operating temperature window is substantially expanded in this work by developing a series of materials with hysteresis-free and tailored transitions at the temperature range of 20–77 K with  $|\Delta S_m| > 0.2 \text{ J cm}^{-3} \text{ K}^{-1}$ . Thus, this discovery can directly lead to the realisation of the AMR system as a great leap toward the application of magnetic cooling technology for hydrogen liquefaction.

In this work, we demonstrate that for  $(Ho)ErCo_2$  compounds, the substitution of Co by particular 3d metal elements, such as Fe or Fe + Ni, can eliminate the hysteresis by avoiding the structural transformation, while maintaining a giant MCE at the transition temperature. Different from the conventional reports, the narrow operating temperature window is substantially expanded in this work by developing a series of materials with hysteresis-free and tailored transitions at the temperature range of 20–77 K with  $|\Delta S_m| > 0.2 \text{ J cm}^{-3} \text{ K}^{-1}$ . Thus, this discovery can directly lead to the realisation of the AMR system as a great leap toward the application of magnetic cooling technology for hydrogen liquefaction.

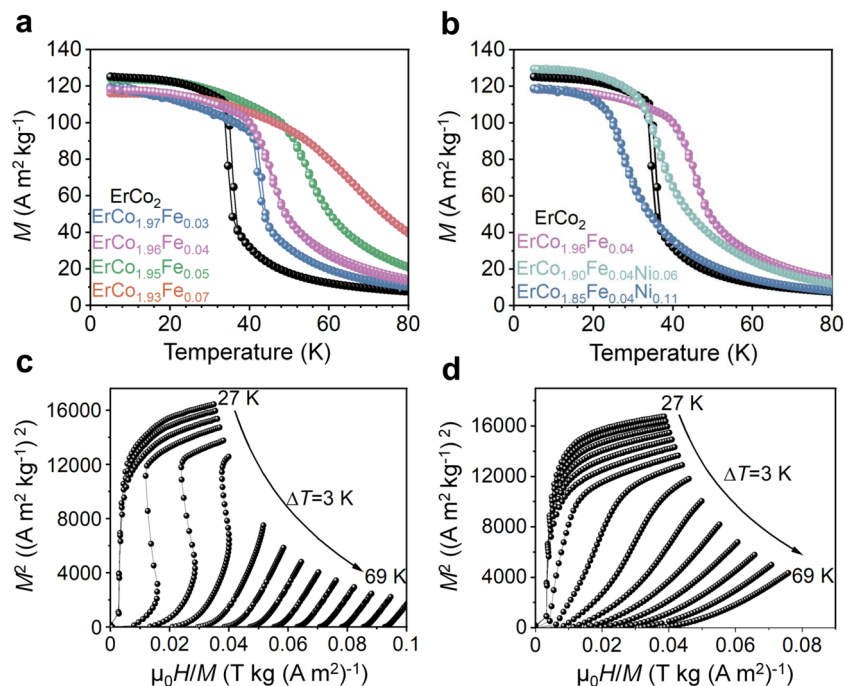


**Fig. 2** Tuning the transition temperature, thermal hysteresis, and order of magnetic phase transition in an  $\text{ErCo}_2$ -based system. **a, b** The Magnetisation ( $M$ ) is plotted versus temperature at an applied magnetic field of 1T showing that the transition temperature can be tuned to higher temperatures (**a**) and to lower temperatures (**b**), while eliminating the hysteresis by substituting Co by Fe and Fe + Ni in the  $\text{ErCo}_2$ -based system. The colours of the curves in **a, b** correspond to the colour of listed alloy compositions. **c, d** The Arrott plots measured from 27 K to 69 K at a temperature step ( $\Delta T$ ) of 3 K for **c**  $\text{ErCo}_2$  and **d**  $\text{ErCo}_{1.95}\text{Fe}_{0.05}$  alloy show the changes of the phase transition from first-order to second-order, respectively.

## Results

### Tuning the transition temperature and thermal hysteresis.

Magnetisation as a function of temperature  $M(T)$  at a magnetic field of 1T is plotted for  $\text{ErCo}_2$  and  $\text{Er}(\text{Co,Fe,Ni})_2$ -based alloys (Fig. 2a, b). The  $\text{ErCo}_2$  alloy itself undergoes the paramagnetic/ferrimagnetic transition at  $T_C = 37$  K that accompanies a magnetostructural phase transition that gives rise to an abrupt change in the magnetisation, and correspondingly induces a giant magnetic entropy change of  $0.37 \text{ J cm}^{-3}\text{K}^{-1}$  (supplementary Fig. 1). This comes at the cost of thermal hysteresis of 2 K (Fig. 2a), hindering the reversibility of MCE and the practical application of these materials. Figure 2a, b show that the partial substitution of Co with Fe or Fe + Ni solves this problem. The elimination of the thermal hysteresis was successfully achieved in the  $\text{ErCo}_{1.96}\text{Fe}_{0.04}$  alloy with a broad transition temperature span, showing the features of SOPT. Further increase of Fe substitution for Co leads to less sharp transitions observed from the  $M$ - $T$  curves and a reduction of magnetic entropy changes, as shown in supplementary Fig. 1. Tunable transition temperature is another requirement of magnetocaloric materials for AMR systems. As observed from Fig. 2a, the transition temperature increased from 37 K to 62 K when  $x$  increased to 0.07 in the  $\text{ErCo}_{2-x}\text{Fe}_x$  alloy while hysteresis was eliminated. The transition temperature can also be tuned toward a lower temperature (28 K) when Ni is alloyed in the  $\text{ErCo}_{1.96}\text{Fe}_{0.04}$  alloy, while maintaining the hysteresis-free state, as shown in Fig. 2b. Refrigeration capacity (RC), defined as the integrated area under the  $-\Delta S_m(T)$  curve at the peak's half value is another important parameter that is a measure for the amount of heat transfer from the cold to the hot reservoirs in a single ideal MR cycle. The RC is improved from  $2.2 \text{ J cm}^{-3}$  for  $\text{ErCo}_2$  to  $2.42 \text{ J cm}^{-3}$  in the case of the  $\text{ErCo}_{1.96}\text{Fe}_{0.04}$  alloy. With a further increase in Fe content, a magnetic entropy change of  $0.17 \text{ J cm}^{-3}\text{K}^{-1}$  at 57 K can be obtained for the  $\text{ErCo}_{1.95}\text{Fe}_{0.05}$  alloy with an enhanced RC of  $2.95 \text{ J cm}^{-3}$ . Although conventionally, a larger RC is achieved at the expense of the peak value of  $-\Delta S_m$ , making the use of magnetic

refrigerants with SOPT less attractive, the  $|\Delta S_m|$  value for the  $\text{ErCo}_{2-x}\text{Fe}_x$  ( $x \geq 0.04$ ) alloys developed in this study induces the largest entropy change of  $0.21 \text{ J cm}^{-3}\text{K}^{-1}$  within the temperature range of 30–77 K compared to all known refrigerant materials without hysteresis reported to date<sup>1,21–24,27,28,31,32</sup>. Arrott plots were employed (Fig. 2c, d) to determine the order of the magnetic phase transitions. A negative slope and reflection points near the transition temperature were observed for the  $\text{ErCo}_2$  alloy, revealing a typical FOPT based on the Banerjee criterion<sup>33</sup>. The negative slope was strongly suppressed, and a characteristic of SOPT was observed for the compositionally-modified  $\text{ErCo}_{1.95}\text{Fe}_{0.05}$  alloy.

**Characterisation of phase transitions.** Although the Arrott plots qualitatively show the nature of the magnetic phase transition, the latter can be investigated further by tracking the change in the crystal lattice during the phase transition. An unambiguous assessment of the phase transition was carried out using in-situ XRD measurement under cryogenic temperatures. The details of the determination of the phase transition by XRD are shown in the supplementary note 1. The change in the lattice spacing upon cooling from 100 to 5 K is plotted in Fig. 3a. Because the quantities  $\sqrt{2}a_r$  and  $c_r/\sqrt{3}$  of the lattice parameters for the rhombohedral phase are equivalent to the  $a_c$  of the cubic lattice,  $\sqrt{2}a_r$  and  $c_r/\sqrt{3}$  for the rhombohedral phase are plotted to compare directly with the lattice parameter of the cubic phase. A step jump in the lattice spacing in  $\text{ErCo}_2$  was observed near the transition temperature for the  $\text{ErCo}_2$  alloy. With Fe substitution for Co in the  $\text{ErCo}_{1.96}\text{Fe}_{0.04}$  alloy, the lattice constant change was substantially reduced, even though a cubic/rhombohedral crystal structure change was observed. This result clearly shows that the addition of Fe can suppress the large volume change that occurs in the magnetostructural phase transition in  $\text{ErCo}_2$  at  $T_{tr}$ . A further increase in Fe content in the  $\text{ErCo}_{1.95}\text{Fe}_{0.05}$  alloy leads to

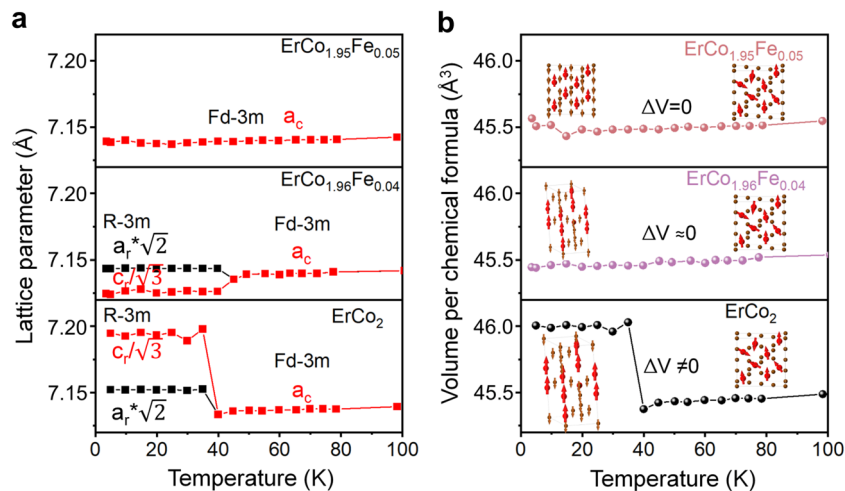


**Fig. 3 Analysis of the lattice constant and crystal volume change around the transition temperature range using cryogenic x-ray diffraction (XRD).** **a** Temperature dependence of the lattice parameters for  $\text{ErCo}_2$ -based alloys. The lattice parameters are obtained from the Rietveld refinement. The lattice parameters of the rhombohedral phase are plotted for  $\sqrt{2}a_r$  (black) and  $c_r/\sqrt{3}$  (red) to compare directly with the lattice parameter of the cubic phase. **b** Temperature-dependent volume per chemical formula for  $\text{ErCo}_2$  (black),  $\text{ErCo}_{1.96}\text{Fe}_{0.04}$  (purple) and  $\text{ErCo}_{1.95}\text{Fe}_{0.05}$  (red) alloys, the crystal structure change upon transition is also illustrated by a unit cell (red and brown spheres represent Er and Co atoms, respectively, and red and brown arrows represent the magnetic moments of the Er and Co atoms, respectively).

no changes in the lattice spacing or volume per chemical formula caused by the structural transition near  $T_{\text{tr}}$ , indicating the realisation of SOPT. In other words, this work demonstrates a concept that the substitution of a  $3d$  metal element, such as Fe for Co in the  $\text{ErCo}_2$ -based Laves phase eliminates the structural phase transition, thereby reducing the thermal hysteresis to 0 K.

A further characterisation of the nature of the phase transitions in  $\text{Er}(\text{Co}_{1-x}\text{Fe}_x)_2$  was performed by measuring the specific heat,  $C$ , using the thermal relaxation method, the details of which are described in the supplementary note 2. In Fig. 4a, the specific heat values given by three measurements are the same in each temperature for the three samples ( $\text{ErCo}_2$ ,  $\text{ErCo}_{1.96}\text{Fe}_{0.04}$  and  $\text{ErCo}_{1.95}\text{Fe}_{0.05}$  alloys), within the experimental accuracy, apart from the temperatures close to the phase transition temperatures. Here, we analysed the dependence of the time evolution of the sample temperature on the phase transition temperatures for the three samples shown in Fig. 4b. For  $\text{ErCo}_2$ , a significant difference in  $T(t)$  was found at the phase transition temperature of  $\sim 35$  K, as indicated by arrow (I) in Fig. 4a. The temperature rise during the first run is significantly suppressed by the existing latent heat, compared to those in the second and third runs. The strong thermal hysteretic behaviour observed in Fig. 2 for the phase transition of  $\text{ErCo}_2$  corresponds to the FOPT behaviour. For sample II ( $\text{ErCo}_{1.96}\text{Fe}_{0.04}$ ), a similar behaviour was observed (Fig. 4b), indicating that the phase transition is still first-order. It is clear that the  $\Delta T_{\text{max}}$  value in the first measurement is lower than those in the second and third measurements. On the other hand, the hysteretic behaviour was not observed within the experimental accuracy in sample III ( $\text{ErCo}_{1.95}\text{Fe}_{0.05}$ ) as shown in Fig. 4b. Thus, we conclude that the phase transitions for  $\text{ErCo}_2$  and  $\text{ErCo}_{1.96}\text{Fe}_{0.04}$  are FOPT, while the  $\text{ErCo}_{1.95}\text{Fe}_{0.05}$  sample does not show FOPT behaviour, which is consistent with that observed by in-situ XRD shown in Fig. 3.

**Origin of large magnetocaloric effect.** Figure 5a shows the results of the specific magnetometric measurements of Er and Co probed by X-ray magnetic circular dichroism (XMCD). Note that the data for the  $\text{ErCo}_2$  alloy were adopted from reference<sup>34</sup>. The Co magnetisation at low temperatures ( $< 10$  K) remains opposite to the Er magnetisation after alloying with Fe, thus revealing that the

ferrimagnetic behaviour is not changed by the substitution of Co with Fe. Unlike for  $\text{ErCo}_2$  alloy that exhibits a sharp change in the magnetic moment of Er at  $T_{\text{tr}}$ , the change in the magnetic moment of Er is more gradual around  $T_{\text{tr}}$ , which is consistent with the  $M$ - $T$  curves presented in Fig. 2. The evolution of the magnetic moments of Er and Co can be directly seen from the XMCD signal shown in the Supplementary Fig. 2. In the XMCD signal of the Co  $L_{2,3}$  edges, an inversion of the edges appears at the temperatures above 56 K, corresponding to the change in the sign of the magnetic moment of Co. For the Er  $M_{4,5}$  XMCD spectra, the intensity of the signal decreases as the temperature increases. In-situ Lorentz microscopy observation in the Fresnel mode was employed to understand the evolution of magnetic domains during cooling. Figure 5b shows the selected micrographs in the cooling process at four different temperatures. These are also marked as i-iv and I-IV in Fig. 5a for  $\text{ErCo}_2$  and  $\text{ErCo}_{1.95}\text{Fe}_{0.05}$  alloys, respectively. For both samples, there is no contrast in the paramagnetic state. The XMCD result in Fig. 5a shows that the magnetic moment of Er atoms increases upon cooling of the  $\text{ErCo}_2$  sample via the magnetic momentum alignment, while the net magnetic moment of Co remains almost zero. This results in the formation of fine and maze-like magnetic domain structures, as shown in ii in Fig. 5b. Note that close to the  $T_{\text{tr}}$  of  $\text{ErCo}_2$ , a mountain-like contrast marked by red circles appears originating from a large strain caused by the cubic/rhombohedral structural transformation. The change in the magnetic domain structure upon cooling to 37 K is due to a substantial increase in the magnetic moment of Er by formation of ferrimagnetic phase, as shown in Fig. 5a. Note that unlike the  $\text{ErCo}_2$  sample, no distinct strain contours were observed in the  $\text{ErCo}_{1.95}\text{Fe}_{0.05}$  sample because the cubic structure was preserved at the temperatures below 52 K in the latter case. The observed transition in the shape of the magnetic domains from II to IV, *i. e.* fine maze-like domain patterns in II, strip-like domain patterns in IV, and their mixture in III (indicated by black arrow heads), are due to the gradual increase in the magnetic moment of Er upon a decrease in temperature without existence of any strain contour. Note that the  $\text{ErCo}_{1.95}\text{Fe}_{0.05}$  phase is in its ferrimagnetic state at the temperature of 10 K.

The giant MCE in the  $\text{ErCo}_2$  alloy originates from the magnetostructural phase transition and itinerant electron metamagnetism (IEM). The latter was proposed by Wohlfarth and

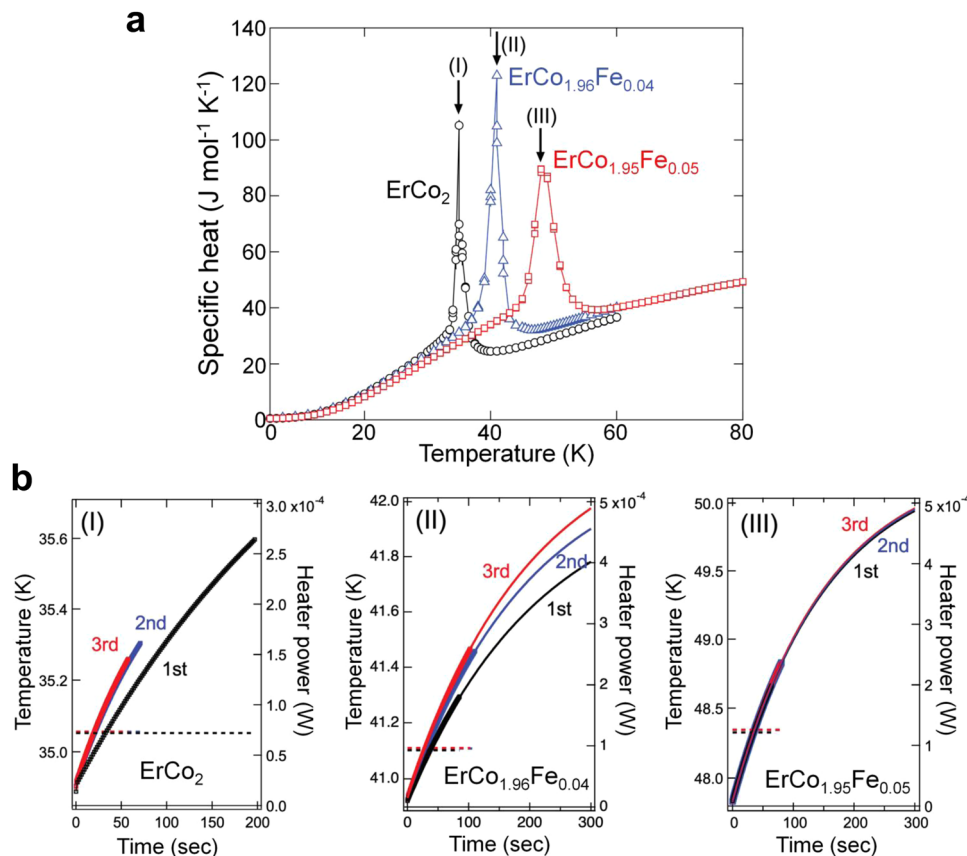


**Fig. 4** Analysis of the latent heat involved with first-order phase transition. **a** Temperature dependence of the specific heat measured by the thermal relaxation method for  $\text{ErCo}_2$  (black),  $\text{ErCo}_{1.96}\text{Fe}_{0.04}$  (blue) and  $\text{ErCo}_{1.95}\text{Fe}_{0.05}$  (red) alloys. **b** Time evolution of the sample temperature obtained using the relaxation method at the temperature where each sample shows a peak anomaly indicated by arrows (I), (II), and (III) in **a**. The dashed lines denote heat power for each measurement (1<sup>st</sup> (black), 2<sup>nd</sup> (blue) and 3<sup>rd</sup> (red) measurements) in **b**.

Rhodes<sup>35</sup>. According to the proposed concept, the creation of a magnetic moment in Co is a consequence of the IEM induced by localised ferromagnetic ordering of Er moments that induces a large exchange field at the transition temperature. This can be observed in Fig. 5a, wherein Co has nearly zero magnetisation in the paramagnetic state, while it antiferromagnetically couples with Er at temperatures below 37 K. In this study, we found SOPT with the substitution of Fe for Co in the  $\text{ErCo}_{1.95}\text{Fe}_{0.05}$  alloy, in which no structural transformation was observed, while a giant MCE was induced. However, based on the XMCD results, the magnetic moment of Co at temperatures below  $T_{\text{tr}}$  remains comparable in  $\text{ErCo}_2$  and  $\text{ErCo}_{1.95}\text{Fe}_{0.05}$  alloys, suggesting that IEM is preserved upon a small substitution of Fe for Co. In addition to the structural transition, any change in the density of states at the Fermi level between these two alloys influences the IEM in Fe-doped alloys<sup>36,37</sup>. We calculated the density of states using density functional theory (DFT) using experimental lattice constants (Supplementary Fig. 3). Trace amounts of Fe substitution for Co have negligible influence on the electronic structure around the Fermi level compared with the cubic/rhombohedral  $\text{ErCo}_2$ . This implies that the instability of the 3d sublattice magnetism and IEM is preserved for the  $\text{ErCo}_{1.95}\text{Fe}_{0.05}$  alloy, which is consistent with the experimental data obtained by XMCD (Fig. 5a). This observation is in contrast to the conventional belief that FOPT results from IEM<sup>36,37</sup>. Here, we demonstrate that by eliminating the structural phase transition, thermal hysteresis can be eliminated, while the giant MCE can still be achieved due to the preserved IEM in the  $\text{ErCo}_{1.95}\text{Fe}_{0.05}$  alloy.

## Discussion

In practical applications, the surface/volume ratio of the magnetic refrigerants should be increased to achieve better heat exchange between the refrigerants and heat-exchanger fluid. Hence, spherical particles are desired. We employed a gas atomisation method and obtained spherical particles with an average particle diameter in the range of 210–350  $\mu\text{m}$ . An example of spherical particles of the  $\text{ErCo}_{1.96}\text{Fe}_{0.04}$  alloy is shown in the inset of Fig. 6a. The optimal annealing of the gas-atomised powders (supplementary Fig. 4) led to the realisation of a  $-\Delta S_m$  value comparable to that of the bulk sample (Fig. 6a). To develop magnetic refrigeration materials suitable for a broad temperature range of 77–20 K, we further investigated different 3d metal dopants to  $\text{ErCo}_2$  and  $\text{HoCo}_2$ -based compounds. We substituted Ni, Al, Fe, and their combinations for Co in  $\text{Er}(\text{Ho})\text{Co}_2$  alloys. Figure 6b shows that hysteresis can be eliminated in conventional FOPT-type  $\text{ErCo}_2$  and  $\text{HoCo}_2$  alloys by the doping, and the transition temperature can be tuned from 20 K to 77 K. These changes enable the values of  $-\Delta S_m > 0.2 \text{ J cm}^{-3} \text{ K}^{-1}$  to be achieved in the range from 20 to 77 K to cover the required temperature range for hydrogen liquefaction (Fig. 6c). The magnetic refrigerants developed in this study yielded significantly larger entropy changes than those of  $\text{HoNi}_2$ <sup>24</sup>,  $\text{HoAl}_2$ <sup>28</sup>,  $\text{REMn}_2\text{X}_2$ <sup>38–40</sup>,  $\text{RECo}_2\text{Mn}_x$ <sup>41</sup> and  $\text{DyAl}_2$ <sup>28</sup> for cryogenic applications, particularly in the temperature range from 30 K to 77 K. For example, the  $-\Delta S_m$  values for the  $\text{ErCo}_{1.85}\text{Ni}_{0.11}\text{Fe}_{0.04}$  and  $\text{HoCo}_{1.8}\text{Ni}_{0.15}\text{Al}_{0.05}$  alloys are 55% and 93% larger than those of  $\text{HoAl}_2$  and  $\text{DyAl}_2$  at the same transition temperatures. Further characterisation of  $\Delta T_{\text{ad}}$  of magnetic refrigerants is depicted in Fig. 6d; above 4 K,

$\Delta T_{ad}$  can be achieved for the magnetic refrigerants developed in this work that can cover the application temperature range from 20 to 77 K for hydrogen liquefaction.

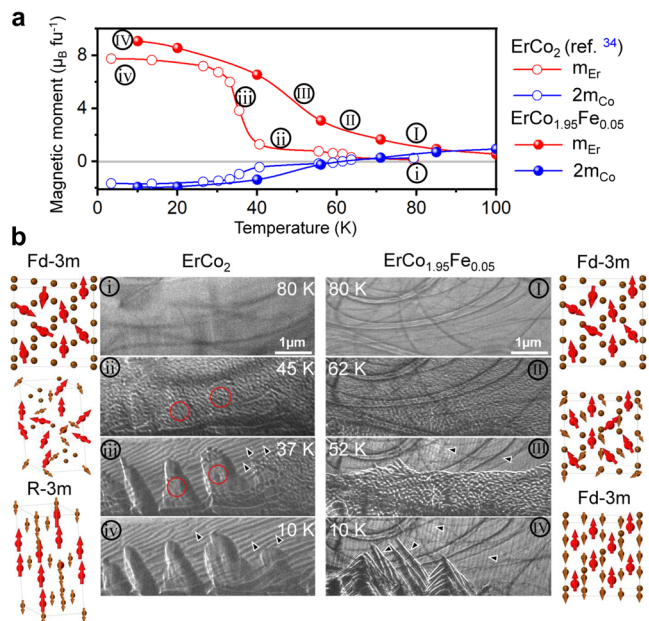


**Fig. 5 Magnetism and magnetic structure for ErCo<sub>2</sub>-based alloys.**

**a** Temperature-dependent magnetic moments for Er (red) and Co (blue) in ErCo<sub>2</sub><sup>34</sup>, and ErCo<sub>1.95</sub>Fe<sub>0.05</sub> alloys. **b** Magnetic domain evolution in ErCo<sub>2</sub>-based alloys examined using cryogenic Lorentz microscopy in the Fresnel mode. The black arrow heads show the magnetic domains and red circles illustrate the mountain-like contrasts caused by strain; the crystal structure change upon transition is also shown by a unit cell (red and brown spheres for Er and Co atoms, respectively, and red and brown arrows for the magnetic moments of Er and Co, respectively).

Hysteresis is a widespread phenomenon resulting from the nature of the first-order phase transition in magnetic refrigerants that leads to the irreversibility of the magnetocaloric response. Herein, we demonstrate that the elimination of hysteresis can be realised by avoiding the crystal structure change across the phase transition, specifically by alloying with 3d elements, while maintaining the giant magnetocaloric effect comparable to that of a conventional FOPT Er(Ho)Co<sub>2</sub> alloy. The role of Fe in suppressing the structural transformation upon phase transition is due to the change from FOPT to SOPT as revealed by in-situ XRD, latent heat measurement, and Lorentz TEM for ErCo<sub>1.95</sub>Fe<sub>0.05</sub>. Moreover, the giant MCE was maintained for SOPT because of the preservation of IEM as found by XMCD experiments and DFT calculations. The Er(Ho)Co<sub>2</sub>-based alloys developed in this study have numerous merits, such as significantly larger magnetic entropy changes compared with those of known materials in the temperature range of 20–77 K, a wide operating temperature window due to the stacking of the refrigerants covering the range of application temperatures for hydrogen liquefaction, easy fabrication, and stable magnetocaloric properties of gas-atomised particles. This may lead to the application of Er(Ho)Co<sub>2</sub>-based alloys for hydrogen liquefaction using an active magnetic regenerator. Moreover, the approach for achieving giant reversible MCE in this study is also expected to be applicable for eliminating the detrimental hysteresis of magnetic refrigerants with FOPT for applications near room temperature, such as Gd<sub>5</sub>Si<sub>2</sub>Ge<sub>2</sub><sup>6–8</sup>, (MnFe)<sub>2</sub>P<sup>9</sup> and La(FeSi)<sub>13</sub>H<sup>14,15</sup>.

## Methods

**Sample preparation.** Polycrystalline (Ho)ErCo<sub>2</sub>-based samples were prepared by arc melting pure constituent elements in an Ar atmosphere, with 2–5 wt.% extra Er and Ho added to compensate the evaporation during sample preparation. The ingots were remelted four times after flipping over to achieve better homogeneity. Thereafter, the ingots were sealed in quartz in an argon atmosphere and annealed for 50 h at 1273 K. The phase constituents and crystal structure were examined by XRD (Rigaku SmartLab 9 kW) with Cu K $\alpha$  radiation in the temperature range of 5–300 K. Thermomagnetic measurements were conducted using a superconducting quantum interference device magnetometer (SQUID-VSM).

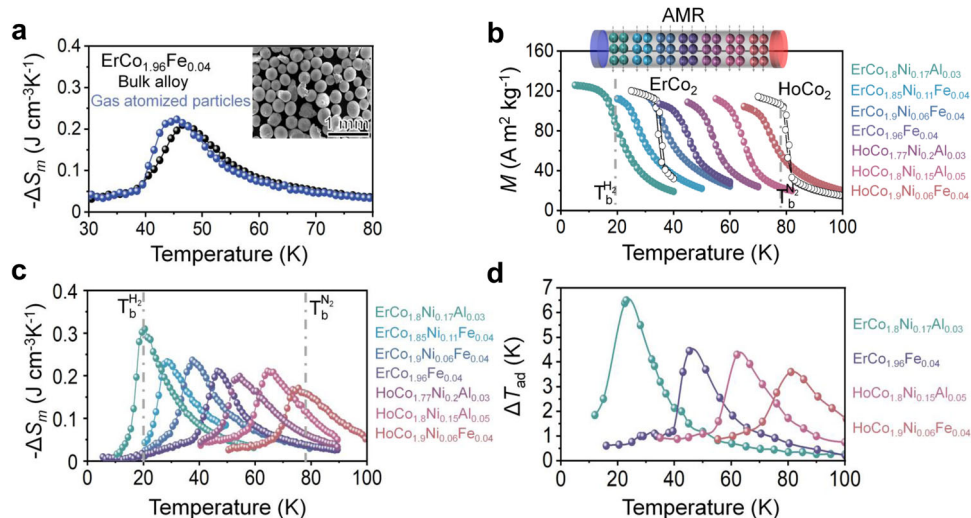


**Fig. 6 Magnetocaloric effects in compositionally engineered (Ho)ErCo<sub>2</sub>-based alloys.** **a** Comparison of the temperature-dependent magnetic entropy change ( $-\Delta S_m(T)$ ) of a bulk sample (black) and gas-atomised (blue) ErCo<sub>1.96</sub>Fe<sub>0.04</sub> particle. The inset shows a scanning electron microscopy (SEM) image of a gas-atomised sample. **b** Temperature-dependent magnetisation  $M(T)$  measurements of the cooling and heating branches from 5 K to 100 K at 1 K intervals ( $\mu_0 H = 1$  T) for a series of magnetic refrigerants with tailored transition temperatures, the spherical particles in AMR with different colours correspond to different magnetic refrigerants with different transition temperatures in **b**. **c** Temperature-dependent magnetic entropy change  $-\Delta S_m(T)$  curves of magnetic refrigerants with tailored transition temperatures covering the large temperature window from 20 K to 77 K. **d** Adiabatic temperature change ( $\Delta T_{ad}$ ) at the field change ( $\Delta H$ ) of 5 T of the selected magnetic refrigerants developed in this work at their transition temperatures. The selected colours of the curves in **b–d** correspond to the colour of listed alloy compositions.

**Thermomagnetic measurements.** To directly measure the adiabatic temperature change, a zirconium oxynitride thin-film Cernox™ thermometer (CX-SD, Lake Shore Cryotronics) was placed on the large surface of a cubic-shaped sample and fixed by thin copper wires. The sample assembly was inserted into the quantum design physical property measurement system (PPMS). The temperature and magnetic field were controlled by PPMS. The sample space was pumped by a cryopump, and the pressure was maintained below  $10^{-4}$  Torr to reach adiabatic conditions. The thermal relaxation method for latent heat measurements was implemented in the physical properties measurement system (PPMS) manufactured by Quantum Design. To evaluate the time evolution of sample temperature during measurement, the raw data were extracted for each measurement.

**Cryogenic microstructure characterisations.** Cryogenic Lorentz microscopy was conducted using ultra-high-voltage (1.2 MV) Hitachi-TEM instrument. The temperature of the TEM specimen was reduced to  $\sim 10$  K in a cryostat TEM sample holder using liquid helium. The specimens for the TEM analysis were prepared by an FEI Helios G4-UX dual-beam system using the lift-out method. The soft XMCD spectra at the Er  $M_{4,5}$  and Co  $L_{2,3}$  edges were recorded using the total electron yield method at the BL25SU beamline of SPring-8. The XMCD signal ( $\mu_m$ ) was obtained as  $\mu_m = (\mu_{+} + \mu_{++}) - (\mu_{-} + \mu_{--})$ , where  $\mu_{+}$  and  $\mu_{-}$  represent the X-ray absorption spectrum (XAS) for the helicity plus ( $h_{+}$ ) and minus ( $h_{-}$ ) of soft X-rays, respectively, and  $\mu_{++}$  and  $\mu_{--}$  respectively represent XAS for a positive and negative applied field with intensity equal to 1.9 T. The degree of circular polarisation was previously estimated as 0.96 at 400 eV<sup>42</sup> and was expected to be similar or larger in the energy region used in the present work. The angle between the magnetic field and the incident X-ray beam was  $10^\circ$  (ref. 43). The rod-shaped sample was fractured in the ultra-high vacuum chamber of the XMCD apparatus with the vacuum level of  $< 5 \times 10^{-7}$  Pa to obtain a fresh surface for the XMCD experiments. The samples were measured at different temperatures between 10 and 100 K. The magnetic moments were calculated using the magneto-optical sum rule analysis for XMCD<sup>44–46</sup> by taking into consideration the spin-correction factor necessary to apply the sum rules for rare earths<sup>47</sup>.

**First-principles calculations.** Density functional theory (DFT) calculations were performed using the full-potential linearised augmented plane wave (FLAPW) method as implemented in the WIEN2K code<sup>48</sup>. The exchange-correlation interaction was approximated using the Perdew–Burke–Ernzerhof (PBE)<sup>49</sup> formulation based on the generalised gradient approximation (GGA). The k-point sampling of the Brillouin zone was performed using  $11 \times 11 \times 11$  k-mesh grids. The spin-orbit coupling (SOC) was included in the calculations self-consistently. The localised 4f electrons of Er were treated based on the implementation of the Hubbard's  $U$  parameter using the DFT +  $U$  method with  $U = 10$  eV and  $J = 0.75$  eV, including the orbital polarisation. The experimental lattice constants for the rhombohedral and cubic structures were used, and Fe doping in  $\text{ErCo}_{1.95}\text{Fe}_{0.05}$  was simulated using the virtual crystal approximation<sup>50</sup>. The ferrimagnetic behaviour and 6  $\mu_B$  orbital moments for Er were confirmed in all systems.

## Data availability

All data are available within the Article and Supplementary Files, or available from the corresponding authors upon reasonable request. Source data are provided with this paper.

Received: 21 September 2021; Accepted: 4 March 2022;

Published online: 31 March 2022

## References

- Gschneidner, K. A. Jr, Pecharsky, V. K. & Tsokol, A. O. Recent developments in magnetocaloric materials. *Rep. Prog. Phys.* **68**, 1479–1539 (2005).
- Franco, V. et al. Magnetocaloric effect: from materials research to refrigeration devices. *Prog. Mater. Sci.* **93**, 112–232 (2018).
- Debye, P. Einige bemerkungen zur magnetisierung bei tiefer temperatur. *Ann. Phys.* **386**, 1154–1160 (1926).
- Giauque, W. F. A thermodynamic treatment of certain magnetic effects. A proposed method of producing temperatures considerably below 1° absolute. *J. Am. Chem. Soc.* **49**, 1864–1870 (1927).
- Giauque, W. F. & MacDougall, D. P. 1933 Attainment of temperatures below 1° absolute by demagnetization of  $\text{Gd}_2(\text{SO}_4)_3 \cdot 8\text{H}_2\text{O}$ . *Phys. Rev.* **43**, 768 (1933).
- Pecharsky, V. K. & Gschneidner, K. A. Jr Giant magnetocaloric effect in  $\text{Gd}_5(\text{Si}_2\text{Ge}_2)$ . *Phys. Rev. Lett.* **78**, 4494–4497 (1997).
- Provenzano, V., Shapiro, A. J. & Shull, R. D. Reduction of hysteresis losses in the magnetic refrigerant  $\text{Gd}_5\text{Ge}_2\text{Si}_2$  by the addition of iron. *Nature* **429**, 853–857 (2004).
- Moore, J. D. et al. Metamagnetism seeded by nanostructural features of single-crystalline  $\text{Gd}_5\text{Si}_2\text{Ge}_2$ . *Adv. Mater.* **21**, 3780–3783 (2009).
- Tegus, O., Brück, E., Buschow, K. H. J. & de Boer, F. R. Transition-metal-based magnetic refrigerants for room-temperature applications. *Nature* **415**, 150–152 (2002).
- Wada, H. & Tanabe, Y. Giant magnetocaloric effect of  $\text{MnAs}_{1-x}\text{Sb}_x$ . *Appl. Phys. Lett.* **79**, 3302–3304 (2001).
- de Campos, A. et al. Ambient pressure colossal magnetocaloric effect tuned by composition in  $\text{Mn}_{1-x}\text{Fe}_x\text{As}$ . *Nat. Mater.* **5**, 802–804 (2006).
- Krenke, T. et al. Inverse magnetocaloric effect in ferromagnetic Ni–Mn–Sn alloys. *Nat. Mater.* **4**, 450–454 (2005).
- Liu, J., Gottschall, T., Skokov, K. P., Moore, J. D. & Gutfleisch, O. Giant magnetocaloric effect driven by structural transitions. *Nat. Mater.* **11**, 620–626 (2012).
- Hu, F. X., Shen, B. G., Sun, J. R. & Cheng, Z. H. Influence of negative lattice expansion and metamagnetic transition on magnetic entropy change in the compound  $\text{LaFe}_{1.4}\text{Si}_{1.6}$ . *Appl. Phys. Lett.* **78**, 3675–3677 (2001).
- Fujita, A., Fujieda, S., Hasegawa, Y. & Fukamichi, K. Itinerant-electron metamagnetic transition and large magnetocaloric effects in  $\text{La}(\text{Fe}_x\text{Si}_{1-x})_{13}$  compounds and their hydrides. *Phys. Rev. B* **67**, 104416 (2003).
- Lyubina, J., Nenkov, K., Schultz, L. & Gutfleisch, O. Multiple metamagnetic transitions in the magnetic refrigerant  $\text{La}(\text{Fe,Si})_{13}\text{H}_x$ . *Phys. Rev. Lett.* **101**, 177203 (2008).
- Jones, L. W. Liquid hydrogen as a fuel for the future. *Science* **174**, 367–370 (1971).
- Numazawa, T., Kamiya, K., Utaki, T. & Matsumoto, K. Magnetic refrigerator for hydrogen liquefaction. *Cryogenics* **62**, 185–192 (2014).
- Monteiro, J. C. B. & Gandra, F. G. Direct measurements of conventional and anisotropic magnetocaloric effect in binary  $\text{RAl}_2$  single crystals. *J. Appl. Phys.* **121**, 213904 (2017).
- Baptista de Castro, P. et al. Machine-learning-guided discovery of the gigantic magnetocaloric effect in  $\text{HoB}_2$  near the hydrogen liquefaction temperature. *NPG Asia Mater.* **12**, 35 (2020).
- Yamamoto, T. A., Nakagawa, T., Sako, K., Arakawa, T. & Nitani, H. Magnetocaloric effect of rare earth mono-nitrides, TbN and HoN. *J. Alloys Compd* **376**, 17–22 (2004).
- Hirayama, Y. et al. Magnetocaloric effect, specific heat and adiabatic temperature change of  $\text{Ho}_x\text{Er}_{1-x}\text{N}$  ( $x = 0.25, 0.5, 0.75$ ). *J. Alloys Compd* **462**, L12–L15 (2008). pp.
- von Ranke, P. J., Grangeia, D. F., Caldas, A. & de Oliveira, N. A. Investigations on magnetic refrigeration: application to  $\text{RNi}_2$  ( $R = \text{Nd, Gd, Tb, Dy, Ho, and Er}$ ). *J. Appl. Phys.* **93**, 4055–4059 (2003).
- Lai, J., Tang, X., Sepehri-Amin, H. & Hono, K. Tuning magnetocaloric effect of  $\text{Ho}_{1-x}\text{Gd}_x\text{Ni}_2$  and  $\text{HoNi}_{2-y}\text{Co}_y$  alloys around hydrogen liquefaction temperature. *Scr. Mater.* **188**, 302–306 (2020).
- Gutfleisch, O. et al. Mastering hysteresis in magnetocaloric materials. *Philos. Trans. R. Soc. A* **374**, 20150308 (2016).
- Guillou, F., Porcari, G., Yibole, H., von Dijk, N. & Bruck, E. Taming the first-order transition in giant magnetocaloric materials. *Adv. Mater.* **26**, 2671–2675 (2014).
- Baptista de Castro, P. et al. Enhancement of giant refrigerant capacity in  $\text{Ho}_{1-x}\text{Gd}_x\text{B}_2$  alloys ( $0.1 \leq x \leq 0.4$ ). *J. Alloys Compd* **865**, 158881 (2021).
- Campoy, J. C. P., Plaza, E. J. R., Coelho, A. A. & Gama, S. Magneto-resistivity as a probe to the field-induced change of magnetic entropy in  $\text{RAl}_2$  compounds ( $R = \text{Pr, Nd, Tb, Dy, Ho, Er}$ ). *Phys. Rev. B* **74**, 134410 (2006).
- Wada, H., Tomekawa, S. & Shiga, M. Magnetocaloric properties of a first-order magnetic transition system  $\text{ErCo}_2$ . *Cryogenics* **39**, 915–919 (1999).
- Zhu, Y. et al. Magnetocaloric effect of  $(\text{Er}_x\text{R}_{1-x})\text{Co}_2$  ( $R = \text{Ho, Dy}$ ) for magnetic refrigeration between 20 and 80 K. *Cryogenics* **51**, 494–498 (2011).
- Zhang, X. X., Wang, F. W. & Wen, G. H. Magnetic entropy change in  $\text{RCoAl}$  ( $R = \text{Gd, Tb, Dy, and Ho}$ ) compounds: candidate materials for providing magnetic refrigeration in the temperature range 10 K to 100 K. *J. Phys. Condens. Matter* **13**, L747 (2001).
- Das, P. K., Bhattacharyya, A., Kulkarni, R., Dhar, S. K. & Thamizhavel, A. Anisotropic magnetic properties and giant magnetocaloric effect of single-crystal  $\text{PrSi}$ . *Phys. Rev. B* **89**, 134418 (2014).
- Banerjee, B. K. On a generalised approach to first and second order magnetic transitions. *Phys. Lett.* **12**, 16–17 (1964).
- Herrero-Albillos, J. et al. Observation of a different magnetic disorder in  $\text{ErCo}_2$ . *Phys. Rev. B* **76**, 094409 (2007).
- Wohlfarth, E. P. & Rhodes, P. Collective electron metamagnetism. *Philos. Mag.* **7**, 1817–1824 (1962).
- Syshchenko, O., Fujita, T., Sechovský, V., Diviš, M. & Fujii, H. Magnetism in  $\text{ErCo}_2$  under high pressure. *Phys. Rev. B* **63**, 054433 (2001).
- Singh, N. K. et al. Itinerant electron metamagnetism and magnetocaloric effect in  $\text{RCO}_2$ -based Laves phase compounds. *J. Magn. Magn.* **317**, 68–79 (2007).
- Wang, J. L. et al. Magnetocaloric effect in layered  $\text{NdMn}_2\text{Ge}_{0.4}\text{Si}_{1.6}$ . *Appl. Phys. Lett.* **98**, 232509 (2011).
- Li, L. W. et al. Giant reversible magnetocaloric effect in  $\text{ErMn}_2\text{Si}_2$  compound with a second order magnetic phase transition. *Appl. Phys. Lett.* **100**, 152403 (2012).
- Wang, J. L. et al. Driving magnetostructural transitions in layered intermetallic compounds. *Phys. Rev. Lett.* **110**, 217211 (2013).
- Gerasimov, E. G. et al. Structure, magnetic and magnetothermal properties of the non-stoichiometric  $\text{ErCo}_2\text{Mn}_x$  alloys. *Intermetallics* **140**, 107386 (2022).

42. Hirono, T., Kimura, H., Muro, T., Saitoh, Y. & Ishikawa, T. Full polarization measurement of SR emitted from twin helical undulators with use of Sc/Cr multilayers at near 400 eV. *J. Electron Spectrosc. Relat. Phenom.* **144–147**, 1097–1099 (2005).
43. Nakamura, T. et al. Development of a soft X-ray magnetic circular dichroism spectrometer using a 1.9 T electromagnet at BL25SU of SPring-8. *J. Electron Spectrosc. Relat. Phenom.* **144–147**, 1035–1038 (2005).
44. Thole, B. T., Carra, P., Sette, F. & Van Der Laan, G. X-ray circular dichroism as a probe of orbital magnetization. *Phys. Rev. Lett.* **68**, 1943–1946 (1992).
45. Carra, P., Thole, B. T., Altarelli, M. & Wang, X. X-ray circular dichroism and local magnetic fields. *Phys. Rev. Lett.* **70**, 694–697 (1993).
46. Chen, C. T. et al. Experimental confirmation of the x-ray magnetic circular dichroism sum rules for iron and cobalt. *Phys. Rev. Lett.* **75**, 152–155 (1995).
47. Teramura, Y., Tanaka, A., Thole, B. T. & Jo, T. Effect of Coulomb interaction on the X-ray magnetic circular dichroism spin sum rule in rare earths. *J. Phys. Soc. Jpn* **65**, 3056–3059 (1996).
48. Schwarz, K., Blaha, P. & Madsen, G. K. H. Electronic structure calculations of solids using the WIEN2k package for material sciences. *Comput. Phys. Commun.* **147**, 71–76 (2002).
49. Perdew, J. P., Burke, K. & Ernzerhof, M. Generalized gradient approximation made simple. *Phys. Rev. Lett.* **77**, 3865–3868 (1996).
50. Bellaiche, L. & Vanderbilt, D. Virtual crystal approximation revisited: Application to dielectric and piezoelectric properties of perovskites. *Phys. Rev. B.* **61**, 7877–7882 (2000).

### Acknowledgements

This work was supported by the JST-Mirai Program Grant Number JPMJMI18A3 and KAKENHI 19H05819, Japan. The synchrotron radiation experiments were performed at BL25SU of SPring-8 with the approval of the Japan Synchrotron Radiation Research Institute (JASRI) (Proposal Nos. 2020A1414 and 2020A2143). Cryogenic Lorentz microscopy was performed using research equipment shared in MEXT Project for promoting public utilisation of advanced research infrastructure (Programme for supporting introduction of the new sharing system), Grant Number JPMXS0410500020. H. Sepehri-Amin and T. Nakamura acknowledge support from NIMS-TOHOKU joint research partnership program. Xin Tang acknowledges the provision of ICYS fellowship.

### Author contributions

X.T. and H.S.A. raised the idea and designed the experiments. X. T. conducted the alloy developments, performed room temperature XRD and magneto-thermal measurement. H.S.A. led the project. H.S.A. and T.O. conducted TEM measurements. N.T. carried out

$\Delta T_{\text{ad}}$  and specific heat measurements. A.M.C., S.K., Y.K. and T.N. performed XMCD measurements and analysed XMCD results. I.K. and Y.Mi. conducted theoretical DFT calculations. H.T. prepared the spherical particles of magnetic refrigerants using gas atomisation process. J.L. contributed in the thermomagnetic measurements and XRD analysis. Y.Ma. carried out in-situ XRD measurements and analysed the data. X.T., H.S.A., N.T. and K.H. interpreted the key findings and wrote the manuscript. All authors discussed the results and commented on the manuscript.

### Competing interests

The authors declare no competing interests.

### Additional information

**Supplementary information** The online version contains supplementary material available at <https://doi.org/10.1038/s41467-022-29340-2>.

**Correspondence** and requests for materials should be addressed to H. Sepehri-Amin.

**Peer review information** *Nature Communications* thanks Jianli Wang and the other, anonymous reviewer(s) for their contribution to the peer review of this work.

**Reprints and permission information** is available at <http://www.nature.com/reprints>

**Publisher's note** Springer Nature remains neutral with regard to jurisdictional claims in published maps and institutional affiliations.



**Open Access** This article is licensed under a Creative Commons Attribution 4.0 International License, which permits use, sharing, adaptation, distribution and reproduction in any medium or format, as long as you give appropriate credit to the original author(s) and the source, provide a link to the Creative Commons license, and indicate if changes were made. The images or other third party material in this article are included in the article's Creative Commons license, unless indicated otherwise in a credit line to the material. If material is not included in the article's Creative Commons license and your intended use is not permitted by statutory regulation or exceeds the permitted use, you will need to obtain permission directly from the copyright holder. To view a copy of this license, visit <http://creativecommons.org/licenses/by/4.0/>.

© The Author(s) 2022